optica

SOFISM: Super-resolution optical fluctuation image scanning microscopy

Aleksandra Sroda,[1,†] Adrian Makowski,[1,†] Ron Tenne,[2,†] Uri Rossman,[2] Gur Lubin,[2] Dan Oron,[2] and Radek Lapkiewicz[1,*]

[1] *Institute of Experimental Physics, Faculty of Physics, University of Warsaw, Warsaw, Poland*
[2] *Department of Physics of Complex Systems, Weizmann Institute of Science, Rehovot, Israel*
**Corresponding author: radek.lapkiewicz@fuw.edu.pl*

Received 4 June 2020; revised 17 August 2020; accepted 24 August 2020 (Doc. ID 399600); published 29 September 2020

Super-resolution optical microscopy is a rapidly evolving scientific field dedicated to imaging sub-wavelength-sized objects, leaving its mark in multiple branches of biology and technology. While several super-resolution optical microscopy methods have become a common tool in life science imaging, new methods, supported by cutting-edge technology, continue to emerge. One rather recent addition to the super-resolution toolbox, image scanning microscopy (ISM), achieves up to twofold lateral resolution enhancement in a robust and straightforward manner. To further enhance ISM's resolution in all three dimensions, we present and experimentally demonstrate here super-resolution optical fluctuation ISM (SOFISM). Measuring the fluorescence fluctuation contrast in an ISM architecture, we obtain images with a ×2.5 lateral resolution beyond the diffraction limit along with an enhanced axial resolution for a fixed cell sample labeled with commercially available quantum dots. The inherent temporal averaging of the ISM technique enables image acquisition of the fluctuation correlation contrast within millisecond-scale pixel dwell times. SOFISM can therefore offer a robust path to achieve high-resolution images within a slightly modified confocal microscope, using standard fluorescent labels and reasonable acquisition times.

https://doi.org/10.1364/OPTICA.399600

1. INTRODUCTION

The diffraction limit poses a fundamental obstacle for far-field fluorescence microscopy, preventing the observation of details finer than about half the wavelength of light [1]. Breakthroughs in biological sample labeling, single molecule spectroscopy, and microscopy setups development allow nowadays routine imaging of objects up to 10 times smaller than the diffraction limit [2–5], e.g., sub-cellular organelles [6]. Highly successful techniques, such as stimulated emission depletion (STED) [2] and localization microscopy [4,5], offer an appreciable resolution enhancement as a trade-off with longer image acquisition times or a more complex imaging setup, respectively. A somewhat different approach is to enable a more modest improvement of resolution but without substantially longer exposure times or added experimental complexity. Image scanning microscopy (ISM) [7,8] and super-resolution optical fluctuation imaging (SOFI) [9] can be considered as examples of the latter category. Such techniques are simpler to adopt in a general microscopy facility and can therefore offer an intermediate approach between the widespread confocal laser scanning microscopy (CLSM) and the more demanding, record-resolution achieving methods.

CLSM is one of the most common modalities for microscopy of biological samples, especially suitable for 3D imaging. In CLSM, the scanned sample is illuminated with a focused laser beam. Fluorescence collected from the sample is imaged onto a small pinhole, which further restricts the sample volume that contributes to the measured signal. The confocal microscope overcomes one of the main limitations of widefield fluorescence microscopy, a strong defocused background overwhelming the observation of a weak focused signal. Such sectioning in the axial direction facilitated 3D imaging of cells, revolutionizing biological microscopy. While in principle CLSM is capable of enhancing the lateral resolution by up to a factor of two, a substantial improvement requires using a small pinhole, drastically reducing the image's signal-to-noise ratio (SNR) [10]. As a result, CLSM images are obtained with a semi-open pinhole and so, practically, their lateral resolution remains limited by the Abbe limit. ISM presents an elegant solution to this issue [7,8], by simply replacing the pinhole with a detector array. Since every pixel in the array is much smaller than the point spread function (PSF) while altogether the array is larger than the PSF's width, up to twofold improved lateral resolution can be achieved without rejecting the fluorescence signal. Although a relatively recent addition to the family of super-resolution techniques, ISM has already become an established method applied in commercial products [11]. Since there are no special requirements from the sample, nor costly additions to the microscope setup, it has been quickly adopted by the life science imaging community [12].

2334-2536/20/101308-09 Journal © 2020 Optical Society of America

Since implementing ISM nowadays is a straightforward task, it is natural to hybridize it with different microscopy and spectroscopy techniques, extending its capabilities. Re-scan confocal microscopy (RCM) [13] and optical photon reassignment microscopy (OPRA) [14] provide all-optical realizations of ISM that alleviate the need for a fast detector array and multiple exposures. Through PSF engineering [15,16] and two-photon excitation [17–20], ISM was extended to achieve a longer depth of field, resistance to scattering, and spectral multiplexing. Alternatively, one can apply the concept of pixel reassignment for the benefit of different types of microscopy contrasts. For example, an ISM setup can provide sharper images in a Raman microscope [21] and map the fluorescence lifetime of dye molecules (FLIM) [22]. Pixel reassignment has even been applied to improve the spatial resolution of ophthalmology [23], where imaged light is back scattered from within the eye.

An alternative image contrast can also be considered as a means to stretch ISM's resolution limit. Relying on nonlinearity due to emitters' saturation, Laporte *et al.* demonstrated enhanced lateral resolution of an ISM image [24]. Increase in resolution in all dimensions was achieved with quantum ISM (Q-ISM), which utilizes photon antibunching, a quantum effect, to generate an image [25]. This method provided (with subsequent image deconvolution) a resolution 2.6 times [26] better than the diffraction limit, however at the price of relatively long image acquisition times. Since the Q-ISM image is collected simultaneously with the standard ISM signal, one can combine the two to alleviate the collection time issue [27].

Temporal fluctuation in the brightness of fluorophores give rise to an alternative source of contrast for super-resolution imaging [4,5]. In particular, SOFI captures super-resolution images by calculating correlation images of naturally blinking emitters such as quantum dots (QDs), dye molecules, and fluorescent proteins [9,28–31]. Although, in principle, an n-fold resolution enhancement can be achieved for the n-th order of correlation, higher-order analysis demands increasingly longer acquisition times. Therefore, second-order correlation images, increasing the lateral resolution by two, are most frequently used. Similar to ISM, implementing SOFI is straightforward since it relies solely on changing the data post-processing [9]. Noting the complementary nature of the resolution enhancement mechanisms of SOFI and ISM, it seems natural to consider a merger of the two methods in order to extend the resolution achieved by each separately.

Here, we experimentally demonstrate a hybrid method that combines SOFI and ISM, termed here SOFISM (super-resolution optical fluctuation image scanning microscopy), realizing a resolution improvement in all three dimensions within standard acquisition times. This concept was theoretically introduced in [32,33] and mentioned in [34], but was not experimentally realized until now. Our analysis reveals the importance of pixel reassignment—sampling the fluctuating scene at several time points—in order to average out noise that is inherent to the fluctuation contrast mechanism. By virtue of this effect, we were able to image a fixed cell sample labeled with QDs within a few-millisecond pixel dwell time. Finally, we demonstrate the acquisition of higher-order SOFISM images by using labels with appropriate fluctuation statistics.

2. SOFISM RESOLUTION IMPROVEMENT

In the following, we describe the theoretical basis of SOFISM resolution improvement as compared to widefield imaging, CLSM, and ISM (described in detail in Supplement 1 Section 1). A flat object, O, contains N point-like fluorescent labels [see Fig. 1(a)] with static positions $\bar{r}_i$ and time-dependent molecular brightness $s_i(t)$ ($i = 1, 2, \ldots, N$). The sample is imaged with a unity magnification imaging system whose PSF is approximated by a Gaussian function with a width parameter σ: $h(\bar{r}, \sigma) \propto \exp(-|\bar{r}|^2/2\sigma^2)$, where $\bar{r}$ is a two-dimensional vector perpendicular to the optical axis. Under uniform illumination, the time-dependent fluorescence signal is a spatial convolution of the object $O(\bar{r}, t)$ and the system's PSF $h(\bar{r}, \sigma)$:

$$F(\bar{r}, t) = O(\bar{r}, t) * h(\bar{r}, \sigma) = \sum_{i=1}^{N} h(\bar{r} - \bar{r}_i, \sigma) s_i(t), \qquad (1)$$

and the obtained widefield image is given by $I(\bar{r}) = \langle F(\bar{r}, t)\rangle_t \propto \sum_{i=1}^{N} h(\bar{r} - \bar{r}_i, \sigma)\langle s_i(t)\rangle_t$, where $\langle \cdots \rangle_t$ denotes time averaging.

In ISM, instead of uniform illumination, the sample is illuminated with a laser beam focused on the optical axis, and the fluorescence signal is recorded by an array of K detectors whose positions are $\bar{r}_a$, $a = 1, 2, \ldots, K$. Neglecting the difference between excitation and emission wavelengths, one can approximate the profile of the focused laser beam [blue-area curve (i) in Fig. 1(b)] with the imaging PSF, h, introduced above. Assuming the detector's diameter is much smaller than σ, the probability of detection versus the emitter's position can also be approximated with a copy of h centered around the detector's position [orange-area curve (ii) in Fig. 1(b)]. The signal collected by each detector is a product of the two PSFs, excitation, and detection, resulting in an effective ISM PSF that is narrower by a factor of $\sqrt{2}$ and shifted to the middle point between the two PSFs, in this approximation. The signal in detector a at scan position $\bar{r}$ can be expressed as

$$F_a(\bar{r}, t) \propto \sum_{i=1}^{N} h\left(\bar{r} - \bar{r}_i - \frac{1}{2}\bar{r}_a, \frac{\sigma}{\sqrt{2}}\right) s_i(t). \qquad (2)$$

Figure 1(c) schematically presents the process of generating ISM and SOFISM images from the raw data ($F_a(\bar{r}, t)$). Producing an ISM image requires three post-processing steps: averaging, pixel reassignment, and image summation. First, the raw data are averaged over the period spent in each pixel in the scan, termed the pixel dwell time, resulting in a scan image per detector: $I_a(\bar{r}) = \langle F_a(\bar{r}, t)\rangle_{\text{pixel}}$. Next, each image is shifted by $-\bar{r}_a/2$ so as to overlap one another (pixel reassignment). Finally, the images are summed together: $I_{\text{ISM}}(\bar{r}) = \sum_{a=1}^{K} I_a\left(\bar{r} + \frac{1}{2}\bar{r}_a\right)$.

In SOFISM, the average of the fluorescence signal is replaced with its correlation (or more precisely its cumulant) at short time delays (for details, see Supplement 1 Section 1). Since, in our analysis, time dependence arises only from the fluctuating molecular brightness, $s(t)$, we focus on its cumulant. The second-order cumulant for a pair of emitters i, j at time delay τ is given by

$$C_{ij}^{(2)}(\tau) \equiv \langle \Delta s_i(t) \Delta s_j(t + \tau)\rangle_t = \delta_{ij} f(\tau), \qquad (3)$$

where $\Delta s_i \equiv s_i(t) - \langle s_i(t)\rangle_t$, δ_{ij} denotes the Kronecker delta function, and $f(\tau)$ is the intensity auto-correlation function.

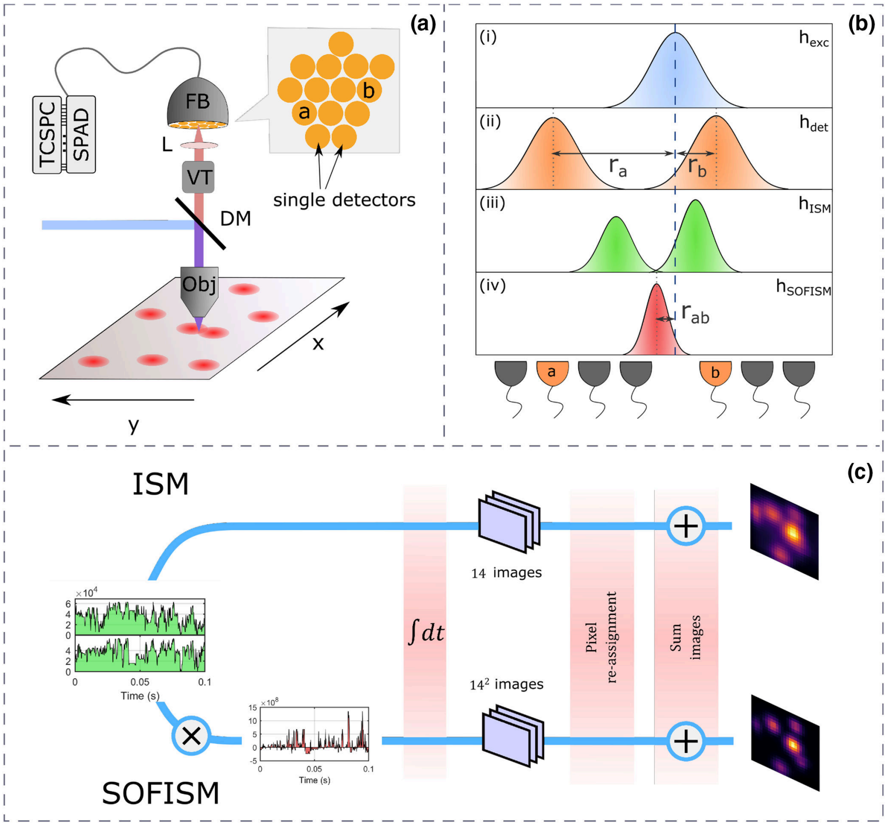

Fig. 1. SOFISM setup and concept. (a) Schematic drawing of the optical setup used in this work. The pinhole in a standard confocal microscope is replaced with a fiber bundle (FB, shown in the inset) routing light into 14 individual single-photon avalanche detectors (SPADs). Obj, objective lens; DM, dichroic mirror; VT, variable telescope; L, lens. (b) Principle of pixel reassignment in ISM and SOFISM. An emitter is most likely to be excited within the extent of the laser profile, h_{exc} [blue area curve in (i)]. The probability of detection is given by a Gaussian centered around the position of each detector, h_{det} [orange area curves in (ii)]. The ISM signal for each detector is a product of the two functions, $h_{\text{exc}} \times h_{\text{det}}$, generating a narrower and shifted effective PSF [green area curve in (iii)]. SOFISM relies on a correlation between two such detectors yielding the h_{SOFISM} PSF shown as a red area curve in (iv). (c) Schematic representation of ISM and SOFISM image generation (noiseless simulation data shown). Integrating over the detection time trace for detector a during a single scan step (green area curve) yields a single pixel value in a stack of 14 scan images. Performing pixel reassignment and summing the stack generates the ISM image. Alternatively, multiplying the fluctuations around the mean of any two time traces (red area curve) and then integrating over time yields a single pixel value in a stack of 14^2 images. As in ISM, performing pixel reassignment and summing the stack produces the final SOFISM image.

Since Eq. (3) assumes that the emitters' intensity fluctuations are independent of one another, only auto-correlations (i.e., when $i = j$) add a non-zero contribution to the cumulant's value. This is a key prerequisite in order for SOFI to resolve nearby emitters. For simplicity, we have assumed here that the fluorescence intensity auto-correlation function of all emitters is identical ($f(\tau)$). Nevertheless, we note that a super-resolved image can be obtained even in the presence of labels with different fluctuation statistics; such variations will factor into the effective brightness of the emitters in the correlation image.

An emitter's intensity auto-correlation, $f(\tau)$, measured at τ well beyond the fluorescent lifetime is typically a positive and decreasing function. As such, a higher SOFI signal is achieved for a shorter sampled time delay. Since the minimal delay is set by the imager's temporal resolution, it is beneficial to employ a fast imager.

A correlation contrast image is constructed by calculating the cumulant at each scan pixel, and for each detector pair, $G^{(2)}_{ab}(\bar{r}, \tau) \equiv \langle \Delta F_a(\bar{r}, t) \Delta \mathrm{F}_b(\bar{r}, t + \tau) \rangle_{\text{pixel}}$, where $\Delta F_n(\bar{r}, t) \equiv F_n(\bar{r}, t) - \langle F_n(\bar{r}) \rangle_{\text{pixel}}$. Plugging Eqs. (2) and (3) into the cumulant definition, we obtain

$$G^{(2)}_{ab}(\bar{r}, \tau) \propto \\ \propto \sum_{i,j=1}^{N} h\left(\bar{r} - \bar{r}_i - \tfrac{\bar{r}_a}{2}, \tfrac{\sigma}{\sqrt{2}}\right) h\left(\bar{r} - \bar{r}_j - \tfrac{\bar{r}_b}{2}, \tfrac{\sigma}{\sqrt{2}}\right) C^{(2)}_{ij}(\tau) \propto \\ \propto \sum_{i=1}^{N} h(\bar{r} - \bar{r}_i - \bar{r}_{ab}, \tfrac{\sigma}{2}) f(\tau). \tag{4}$$

The remaining two steps to achieve a SOFISM image [bottom part of Fig. 1(c)] are identical to the ones described above for ISM: pixel reassignment and image summation. Noting that the image stack contains now an image for each detector pair translated by $\bar{r}_{ab} \equiv \frac{\bar{r}_a + \bar{r}_b}{4}$ [see Fig. 1b(iv)], a final SOFISM image can be formed as $G^{(2)}(\bar{r}, \tau) = \sum_{a,b=1}^{K} G^{(2)}_{ab}(\bar{r} + \bar{r}_{ab}, \tau)$.

In general, imaging the n-th order cumulant in this method can increase the resolution by $\sqrt{2n}$. Subsequent image deconvolution [also termed Fourier reweighting (FR)] can further increase the resolution, by up to a factor of $2n$, by digitally amplifying high spatial frequencies in the recorded image [8]. It should be noted, however, that the improvement due to FR depends on the SNR at these high spatial frequencies.

We note that while the above discussion is limited to two dimensions, SOFISM is inherently compatible with 3D scanning.

In fact, as shown below, *z*-sectioning—the rejection of out-of-focus emission—in SOFISM outperforms both CLSM and ISM providing roughly a twofold enhancement in axial resolution. Supplement 1 Section 2 contains a full mathematical description of 3D resolution in SOFISM.

3. EXPERIMENTAL DEMONSTRATION OF SOFISM

A schematic of the optical setup used in the current work (similar to the one used in [25]) is shown in Fig. 1(a) (for details, see Supplement 1 Section 3). Briefly, a pulsed laser beam (either 473 nm or 515 nm wavelength) focused by a high-numerical-aperture objective (NA = 1.4) excited a fluorescent sample placed on a piezo stage. Fluorescence from the sample was collected by the same objective, spectrally filtered by a dichroic mirror and a long-pass filter, and imaged on a fiber bundle. Light from 14 of the fibers was directed to separate single-photon avalanche detectors (SPADs) whose outputs are connected to a time-correlated single-photon-counting (TCSPC) module that recorded the photon arrival times. In order to calculate cumulants, the acquired time tags from each detector, during a pixel dwell time (typically 100 ms), were divided into finer time bins of less than 200 µs duration.

To demonstrate the resolution improvement of SOFISM, we imaged a sample of colloidal QDs (Qdot 625, Thermofisher, referred to as QD1 in the remainder of this text) sparsely spread on a microscope coverslip (see Supplement 1 Section 4 for sample preparation protocol). Figure 2 compares the performance of SOFISM with that of CLSM, ISM, and the recently introduced Q-ISM method, both with and without image deconvolution. The details of constructing the different images from raw data are given in Supplement 1 Section 3.

Temporal fluctuations in the emission intensities manifest in the form of dark lines in the vertical direction (scan direction) of the CLSM image [Fig. 2(a)]. These fluctuations, which add noise to the CLSM image, are in fact the basis for image enhancement in the SOFI analysis. Apart from appearing sharper than the CLSM image, the ISM image [Fig. 2(b)] features a reduced level of noise due to temporal fluctuations during the scan. This noise reduction occurs since the value of each pixel is a sum of contributions from all detectors in the array, sampling the scene at different times. That is, since scan images of different detectors are shifted before summation, the contributions of different detectors to a specific image pixel are taken from entirely different pixel dwell periods, which can be hundreds of milliseconds apart. In contrast, without pixel reassignment, a CLSM image is a sum of simultaneously measured signals of different detectors.

One option to achieve an enhanced resolution is by performing a Q-ISM analysis [Fig. 2(c)] [25]. Using the fact that each label is inherently a single-photon-at-a-time emitter, one can generate an image whose contrast is the lack of photon pairs, termed photon antibunching. We note that while Q-ISM and SOFISM share many experimental attributes, the contrast mechanism of Q-ISM is very different, namely, it does not rely on intensity fluctuations of the fluorophores but on quantum correlations in their emission. As a result, Q-ISM requires faster detectors and generally suffers from a lower SNR, as compared with SOFI imaging. Despite these differences, both Q-ISM and SOFISM images produce identical PSFs. A comparison of SNR for the two techniques is further explored in Section 5.

The result of SOFISM analysis is shown in Fig. 2(d), providing a resolution improvement similar to Q-ISM. The comparison of interpolated cross sections across two emitters [Fig. 2(e)] provides a clearer demonstration of the resolution improvement. To achieve further sharpening, FR was applied to the ISM, Q-ISM, and SOFISM images [Figs. 2(f)–2(h), respectively], flattening the spatial frequency response of the PSF by amplifying higher frequencies. Similar to the non-deconvolved images, FR Q-ISM [Fig. 2(g)] and FR SOFISM [Fig. 2(h)] yield comparable resolutions.

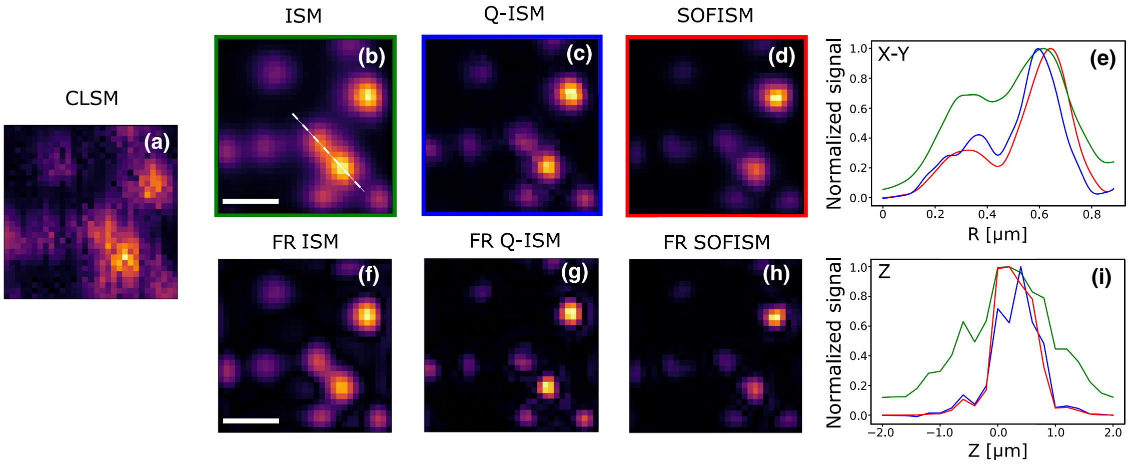

Fig. 2. Resolution improvement performance of SOFISM. A 1.5 µm × 1.5 µm confocal scan (50 nm steps, 100 ms pixel dwell time, ∼96 s for the entire scan, 0.5 µW excitation power) of a sparse sample of QD1 quantum dots. (a) CLSM: the summed intensity over the whole detector array per scan position. (b) ISM: the image of each detector is shifted before summation. (c) Q-ISM: the antibunching signal is shifted prior to summation (see Sections 1 and 3 of the supplementary material in [25]). (d) Second-order SOFISM image: correlations between every two detectors are computed and shifted prior to summation. A temporal binning of 0.2 ms is used to calculate the correlation here. (e) Comparison of interpolated cross sections across the dotted white line shown in (b) for ISM (green), Q-ISM (blue), and SOFISM (red). (f)–(h) Fourier reweighted (deconvolved) images of (b)–(d), respectively. (i) Z-scan: a different region in a flat QD sample was imaged in a few defocus conditions (see Supplement 1 Fig. S7). The collected signal, integrated over the entire image, is presented as a function of objective axial position for ISM (green), Q-ISM (blue), and SOFISM (red). See Supplement 1 Fig. S7 for full scan details. Scalebars are 0.5 µm.

By fitting multiple images of isolated QDs, we estimate the mean resolution gain of the different methods (see Supplement 1 Section 5). ISM, SOFISM, and FR SOFISM provide a 1.3 ± 0.1, 1.7 ± 0.1, and 2.5 ± 0.3 enhancement factor over the diffraction limit, respectively. It is likely that the finite size of our detectors (fibers), non-identical excitation and detection PSFs, and spatial drift can account for the lower enhancement factors compared to those predicted in theory.

In order to test the z-sectioning capability of SOFISM, we performed multiple confocal scans of a different area in a similar QD sample at different positions of the focus with respect to the sample (see Supplement 1 Fig. S7). Figure 2(i) shows the integrated intensity of images versus the objective position for ISM (green), Q-ISM (blue), and SOFISM (red), peaking around $z = 0$. The narrower peaks for SOFISM and Q-ISM demonstrate that the contrast contribution of out-of-focus emitters is much smaller than in the case of CLSM and ISM, yielding a higher resolution in the z direction. For a quantitative estimate, we fitted all curves with a Gaussian function, obtaining FWHM values of 1.6 μm for ISM and 0.8 μm for both Q-ISM and SOFISM. These values indicate a longitudinal resolution improvement of ∼2 for both Q-ISM and SOFISM with respect to ISM.

4. IMAGING A BIOLOGICAL SAMPLE WITH SOFISM

To show the applicability of SOFISM in bio-imaging, we demonstrated imaging of a sample of 3T3 cells whose microtubules were labeled with QD1 (see Supplement 1 Section 6 for sample preparation protocol).

Figure 3 presents a comparison among CLSM (3a), ISM (3b), SOFISM (3c), and FR SOFISM (3d) images generated from a representative scene of a 3 μm × 3 μm area with a scan pixel dwell time of 50 ms. To obtain a reasonable field of view within a few seconds exposure time, characteristic of super-resolved image acquisition, one would require a pixel dwell time in the millisecond range. In order to test the feasibility of such short pixel dwell times, we produced FR SOFISM images from the same scan data sets truncated (in post-processing) to a duration of 1 ms, 5 ms, 15 ms, and 25 ms per scan step [Figs. 3(e)–3(h), respectively]. We note that most of the features that appear in the full dwell time image are already clearly resolved with a 5 ms dwell time. This dwell time approaches the standard pixel acquisition times in a confocal microscope, around 1 ms.

5. EFFECT OF THE PIXEL REASSIGNMENT ON SNR

As demonstrated in Fig. 2, one of the benefits of performing imaging in an ISM architecture is the reduction of noise due to temporal fluctuations. Figure 4 explores the increase in SNR due to pixel reassignment for Q-ISM and SOFISM and for various pixel dwell times.

For this purpose, we scan a 1.5 μm × 1.5 μm scene from a sparse sample of core/shell/shell CdSe/CdS/ZnS QDs, termed here QD2 (synthesis details can be found in the supplementary information of [25,35]). By truncating the data traces so that the time per scan step is 1, 3, 10, 30, or 100 ms, we examine the effect of the pixel dwell time on the SNR of Q-ISM and SOFISM images alongside their nonpixel reassigned variations.

The first row of images in Fig. 4 presents CLSM images with increasing pixel dwell time from left to right (times given on top of each column). The second and fourth rows show the nonpixel-reassigned versions of Q-ISM and SOFISM, i.e., the total signal of antibunching and second-order intensity cumulant per scan step. Surprisingly, although antibunching is generally considered to be a fainter and more difficult signal to measure, the SNR of both images is similar (see Supplement 1 Section 7 and Supplement 1 Fig. S8 for pixel-wise SNR analysis results). Indeed, a more careful analysis of the signal produced from a static measurement of a single QD, presented in Supplement 1 Section 7 (Supplement 1 Fig. S10), shows that for short exposure times, the SNR of the

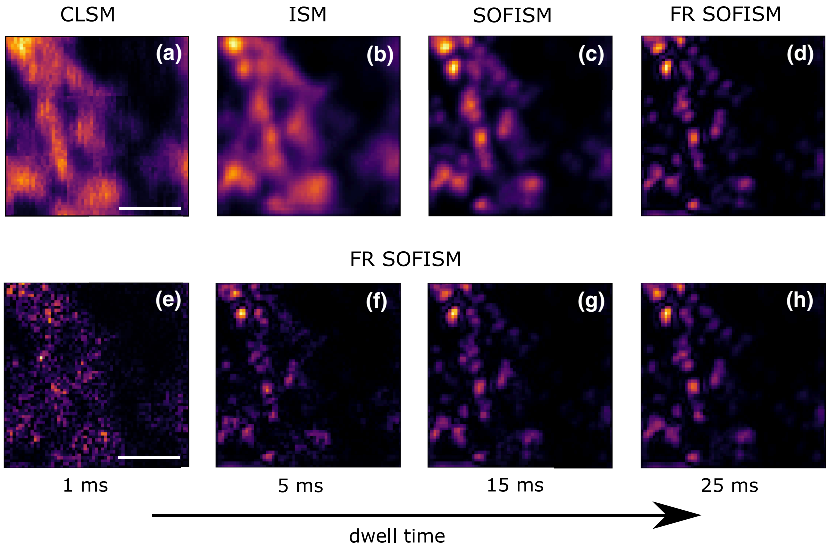

Fig. 3. SOFISM images of microtubules in a fixed cell sample. A 3 μm × 3 μm confocal scan (step size 50 nm, pixel dwell time 50 ms, ∼186 s for the entire scan, 7 μW excitation power) of microtubules in a fixed 3T3 cell labeled with QD1 quantum dots analyzed in multiple ways: (a) CLSM, (b) ISM, (c) SOFISM, and (d) Fourier reweighted (FR) SOFISM. (e)–(h) Comparison of FR SOFISM images for 1 ms (e), 5 ms (f), 15 ms (g), and 25 ms (h) acquisition time per scan step. To compare the quality of SOFISM at different pixel dwell times while using the same data set, we truncate the data acquired in each pixel so that its duration matches the specified scan step dwell time. Scalebar [in both (a) and (e)], 1 μm.

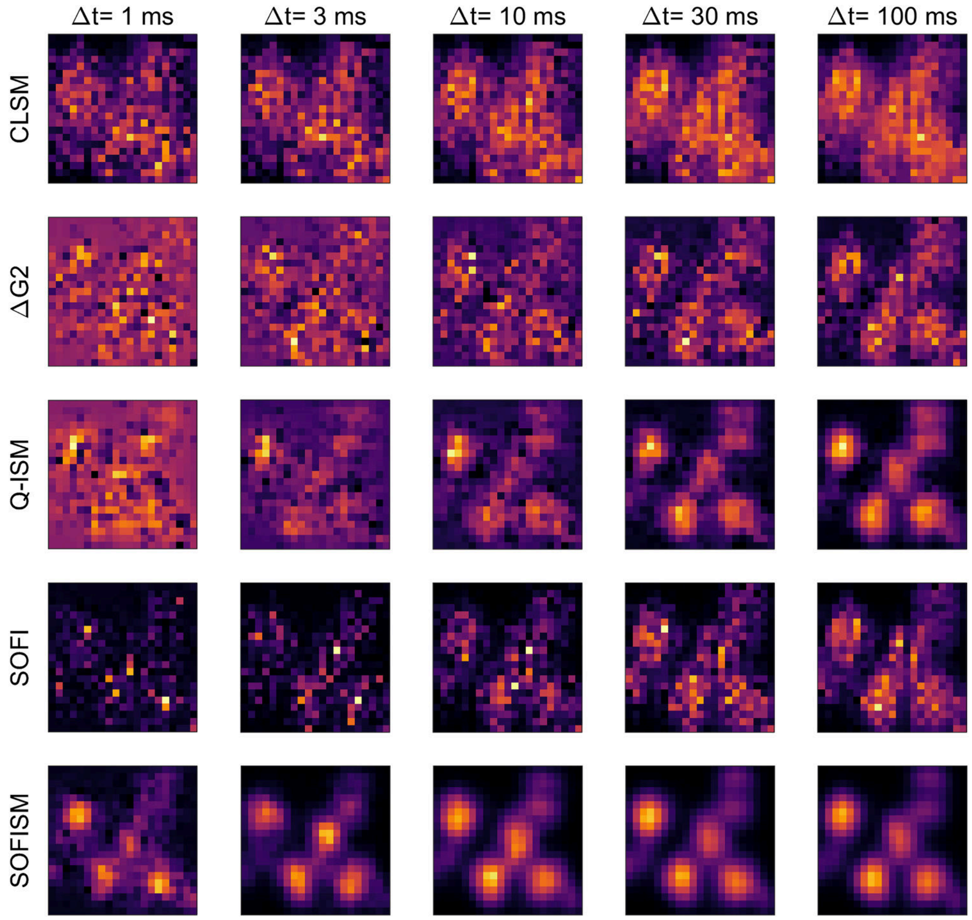

Fig. 4. Effect of pixel reassignment on image SNR for various dwell times. A 1.5 μm x 1.5 μm confocal scan (50 nm steps, 200 ms total pixel dwell time, ~192 s for the entire scan, 4.5 μW excitation power) of a sample of QD2. The effective pixel dwell time (obtained by truncating the data in post-processing) is given at the top of each column. Each row contains images obtained with a different technique: CLSM (first row), summed antibunching—$\Delta G2$ (second row), Q-ISM (third row), summed SOFI (fourth row), and SOFISM (fifth row). In the context of this figure, SOFI refers to a SOFI correlation analysis applied to scan data without pixel reassignment.

SOFI and antibunching contrasts are very similar. While this may seem unintuitive, one should take into account that the fluctuation periods in many types of emitters can occur on a millisecond time scale and even beyond. Thus, estimating the correlation of these fluctuations during a specific short period may strongly bias the estimate.

Indeed, apart from an improved resolution, the pixel reassigned Q-ISM images (third row of Fig. 4) demonstrate an increased SNR compared to the nonpixel reassigned analysis of the same data (first row). However, the same comparison for the SOFI fluctuation contrast produces a substantially more prominent effect. SOFISM images, shown in the fifth row of Fig. 4, achieve a reliable image of the scene even with few-millisecond exposure time, whereas the equivalent SOFI images seem to contain very little information. A more quantitative analysis of this phenomenon is given in Supplement 1 Fig. S8, showing that the SNR of the SOFISM image is roughly ×3 better than the SOFI image of the same scene, for a 3 ms pixel dwell time.

We attribute the stark improvement in SNR to the natural averaging provided by the ISM setup. Pixel reassignment sums the contributions of multiple detector pairs, sampling the same scene at different times. While this averaging effect enhances the quality of all scanned images (ISM and Q-ISM), a contrast based on fluctuations stands to benefit even more. Without pixel reassignment, a SOFI image estimates the cumulant from a specific realization of the random fluctuation signal, which may, for example, contain only the bright state. In contrast, the SOFISM analysis sums contributions from multiple realizations separated by up to hundreds of milliseconds. We posit that it is this averaging mechanism that enables the formation of quality SOFISM images shown in Fig. 3 even at short pixel dwell times.

6. IMAGING WITH HIGHER-ORDER CORRELATIONS

As described in Section 2 of this text, a deconvolved n-th order SOFISM image should, in principle, exhibit a lateral resolution $2n$ times below the diffraction limit. However, for a typical intensity distribution induced by blinking, the SNR of the image drastically reduces with increasing correlation orders and requires substantially longer acquisition times.

Figures 5(a)–5(c) show the second-, third-, and fourth-order SOFISM images generated in post-processing from a single scan of a QD1 sample (see Supplement 1 Section 3 for analysis details). Higher-order cumulants typically present lower SNR

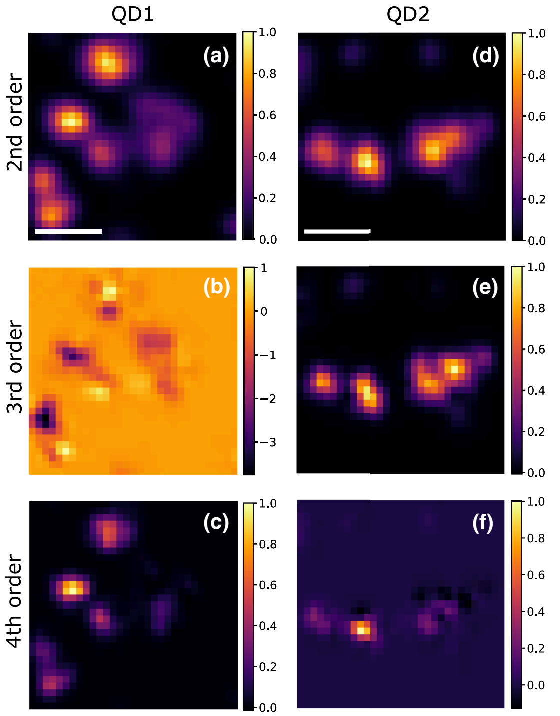

Fig. 5. Demonstration of higher-order SOFISM. Two 1.5 μm × 1.5 μm confocal scans [50 nm step size, 90 ms pixel dwell time divided to 0.2 ms bins, ~96 s for the entire scan, excitation power: 2 μW for (a)–(c) and 9 μW for (d)–(f)] on two different types of quantum dots: QD1 with two fluorescent intensity states: a bright on state and a dark off state [second-, third-, and fourth-order SOFISM images in (a)–(c), respectively] and QD2 with an additional gray state [second-, third-, and fourth-order SOFISM images in (d)–(f), respectively]. Note that for the fourth-order SOFISM, images display the fourth-order cumulant multiplied by −1. Scalebar in both (a) and (d) is 0.5 μm long. Each of the images (a)–(f) was normalized to its maximal pixel value.

and are, therefore, more sensitive to the presence of a correlation background. Since oscillations in the position of the sample piezo-stage are a source of such excess correlations, we filter out several oscillation-prone spectral components in the fluorescence intensity traces (see Supplement 1 Section 3). Filtering has a minute effect on the third- and fourth-order SOFISM images and no apparent effect on second-order SOFISM images. We therefore exercise it only for third- and fourth-order analysis.

Indeed, even-ordered cumulant analysis [Figs. 5(a) and 5(c)] produces clear super-resolved images with the fourth order presenting a higher resolution albeit with a lower SNR. A quantitative analysis yields relative resolution enhancements of 2.5 ± 0.3 and 4.0 ± 0.7 as compared to the diffraction limit, for second- and fourth-order FR SOFISM, respectively (see Supplement 1 Section 5). However, while a reasonable second-order SOFISM image was obtained for all tested scenes, due to the noise sensitive estimation of the fourth-order cumulant, some data sets did not produce a reliable fourth-order SOFISM image.

Surprisingly, even measurements that resulted in a reliable fourth-order SOFISM image could not produce sensible third-order SOFISM images. Such noisy images, containing positive and negative valued neighboring pixels [Fig. 5(b)], suggest that the third-order cumulant cannot be well estimated within the short pixel dwell time in this case. While we find this observation difficult to explain, we suggest that it is an inherent issue for standard QDs, for whom the switching time scales can be on the order of the pixel dwell time (see Supplement 1 Fig. S14). The colloidal QDs used here (QD1) are a prime example of this case, switching from a bright on state to a dark off state with durations that can reach several seconds (blinking analysis presented in Supplement 1 Fig. S14). In such a case, the sign of the measured third-order correlation depends on which state is more common during the specific sampling period (see Supplement 1 Section 8). Since even relatively bright QDs, such as QD1, spend a substantial fraction of the measurement time in each state, the mean value of the third-order cumulant is close to zero, and only very long sampling times can yield reasonable SNR SOFI images (see Supplement 1 Fig. S14).

Therefore, in order to achieve meaningful third-order SOFISM images within a short pixel dwell time, it is reasonable to use fast switching emitters. In the past decade, there have been several reports of QDs showing a third, gray, state in which the brightness drops to a level of around 20% of the on-state emission brightness [36–38]. In some cases, it was shown that switching between the on and gray states occurs on a time scale of up to 10 ms [38].

To demonstrate the effect of an additional gray state on the SOFI contrast, Figs. 5(d)–5(f) present the second-, third-, and fourth-order SOFISM images of a typical scene taken from a sparse sample of QD2 that has such a gray state (see Supplement 1 Fig. S14). The third-order SOFISM image of QD2 presents a credible image with a clear sign of the cumulant, an improved resolution, and a reasonable SNR.

To further explore the advantage of using emitters exhibiting an additional emitting state, Supplement 1 Fig. S14 takes a closer look at the fluorescence intensity dynamics of a single QD2 emitter. Under near saturation illumination conditions, these QDs switch between the on and grey states within a <10 ms timescale. These rapid fluctuations contribute to the acquisition of third-order SOFI signal in two ways. First, the faster switching times allow a more precise estimation of cumulants within the pixel dwell time. Furthermore, the presence of a third state, whose intensity is close to the dark off state, skews the intensity distribution function, thus generating an appreciable third-order moment for the distribution, critical for third-order SOFI (see theoretical analysis in Supplement 1 Fig. S13) [39].

7. DISCUSSION

Imaging with SOFISM is compatible with a typical ISM system, provided that the sample fulfills the conditions required by the SOFI technique [9]. First, fluorophores must exhibit temporal fluctuations in their emission probability, independent of one another. As mentioned above, this is not a severe limitation since the fluorescent intensity of different types of QD, dye molecules, and fluorescent proteins naturally fluctuates [30,31]. Second, special attention must be given to the stability of the excitation source, detection system, and sample position. Fluctuations in these parameters may contribute a false positive SOFI contrast, overwhelming the correlation due to fluorescence intermittency.

SOFISM has the potential to improve the resolution obtained in ISM in three dimensions with standard fluorescent labels and without relying on long exposure times. In contrast to Q-ISM [25] and saturation ISM [24], the acquisition of a reasonable SNR image requires only a few milliseconds per pixel, as compared to circa 100 ms in the case of Q-ISM. A potential for higher performances with the same experimental technique may be possible with the assistance of advanced analysis algorithms. While here we adopt a relatively basic approach, there are multiple advanced SOFI analysis methods [40–44]. Furthermore, there are alternative approaches to analyze fluorescence fluctuations [45,46] that may be appropriate here; one of those was even recently implemented in an ISM architecture [47].

While the current work employs QDs, uncommon as fluorescent labels in biological microscopy, it is reasonable that SOFISM can be performed with organic dye molecules and fluorescent proteins as contrast agents. Widefield SOFI imaging has been performed with both organic dye labels [30] and photochromic fluorescent proteins [28,48]. The use of low-noise, high-temporal-resolution avalanche detector arrays enables access to the fastest fluctuation dynamics typical of organic dyes [49], which cannot be captured with standard cameras. Moreover, since shot noise is not the main source of noise, SOFISM may be performed under relatively low excitation powers, avoiding the photo-bleaching of organic fluorescent labels.

In order to extend the imaging field of view without increasing the scan time, methods that parallelize the data collection process should be employed. One option would be to perform SOFISM with a multi-focal setup, where multiple laser beams and a large detector array are used. In this way, a substantial portion of a sample can be covered at once, drastically shortening the acquisition process. This concept was already realized within the scope of ISM [50]. Such a technique requires a fast and sensitive imaging device, such as SPAD arrays, whose performances witnessed great advancements in the past decade [51].

Alternatively, simultaneous acquisition of a large field of view can be realized by imaging correlations under a structured illumination (SIM) [52]. Such a concept can alleviate the need for extremely fast detectors since scanning is not required. To reduce the degrading effects of scattering and aberrations, one can perform SIM in a quasi-random manner, as done in the blind SIM (or rSIM) method [53–57]. Blind SIM applies multiple unknown illumination patterns containing high spatial frequencies at the object plain to reconstruct a widefield super-resolved image. In fact, some of the algorithms that interpret blind SIM derive inspiration from SOFI, using temporal and spatial correlations in order to reconstruct the object [57,58]. However, there is a fundamental difference between such approaches and SOFISM, in terms of both the super-resolution mechanism and the limits of its resolution enhancement. SOFISM derives its resolution enhancement from two sources: correlations in temporal fluctuations (SOFI) and a SIM (ISM). It is the combination of the two mechanisms that yields a ×4 resolution enhancement for second-order correlation. In comparison, blind SIM is a clever manner to perform SIM and as such is limited to a factor of ×2 improvement in resolution, just as SIM. Combining multiple unknown illumination patterns (blind SIM) together with fluctuations in the sample fluorescence (SOFI) would increase the spatial frequency cutoff of the raw data, much like the combination of SOFI and ISM in this work. This should enable a widefield reconstruction of a super-resolved image beyond the resolution limit of both SIM and SOFI.

8. CONCLUSION

We have demonstrated here a robust method to increase the resolution of an ISM microscope beyond a ×2 enhancement of the diffraction limit by utilizing brightness fluctuation correlation as the image contrast. In the current demonstration, the method, termed SOFISM, achieved 2.5 ± 0.3 fold resolution improvement in second-order FR SOFISM. Super-resolved images of a fixed cell sample, captured within a few-millisecond pixel dwell time, highlight the potential of SOFISM to produce reliable images within the standard time scales of confocal microscopy.

Funding. European Research Council (ColloQuantO); Crown Photonics Center; Minerva Foundation; KLA-TENCOR Corporation; Narodowe Centrum Nauki (2015/17/D/ST2/03471); Ministerstwo Nauki i Szkolnictwa Wyższego; Foundation for Polish Science under the FIRST TEAM project ‘Spatiotemporal photon correlation measurements for quantum metrology and super-resolution microscopy’ co-financed by the European Union under the European Regional Development Fund (POIR.04.04.00-00-3004/17-00).

Acknowledgment. The authors thank Y. Ebenstein for the preparation of biological samples, S. Itzhakov for synthesizing the quantum dots used in this work, and W. Kondrusiewicz, M. Pawłowska, J. Oracz, A. Krupinski-Ptaszek, and P. Fita for discussions about the work and the paper.

Disclosures. The authors declare no conflicts of interest.

See Supplement 1 for supporting content.

† These authors contributed equally to this work.

REFERENCES

1. E. Abbe, “Contributions to the theory of the microscope and the microscopic perception (translated from German),” Arch. Mikr. Anat. **9**, 413–468 (1873).
2. S. W. Hell and J. Wichmann, “Breaking the diffraction resolution limit by stimulated emission: stimulated-emission-depletion fluorescence microscopy,” Opt. Lett. **19**, 780–782 (1994).
3. M. G. L. Gustafsson, “Surpassing the lateral resolution limit by a factor of two using structured illumination microscopy,” J. Microsc. **198**, 82–87 (2000).
4. M. J. Rust, M. Bates, and X. Zhuang, “Sub-diffraction-limit imaging by stochastic optical reconstruction microscopy (STORM),” Nat. Methods **3**, 793–795 (2006).
5. E. Betzig, G. H. Patterson, R. Sougrat, O. W. Lindwasser, S. Olenych, J. S. Bonifacino, M. W. Davidson, J. Lippincott-Schwartz, and H. F. Hess, “Imaging intracellular fluorescent proteins at nanometer resolution,” Science **313**, 1642–1645 (2006).
6. S.-H. Shim, C. Xia, G. Zhong, H. P. Babcock, J. C. Vaughan, B. Huang, X. Wang, C. Xu, G.-Q. Bi, and X. Zhuang, “Super-resolution fluorescence imaging of organelles in live cells with photoswitchable membrane probes,” Proc. Natl Acad. Sci. USA **109**, 13978–13983 (2012).
7. C. J. R. Sheppard, “Superresolution in confocal imaging,” Optik **80**, 53–54 (1988).
8. C. B. Müller and J. Enderlein, “Image scanning microscopy,” Phys. Rev. Lett. **104**, 198101 (2010).
9. T. Dertinger, R. Colyer, G. Iyer, S. Weiss, and J. Enderlein, “Fast, background-free, 3D super-resolution optical fluctuation imaging (SOFI),” Proc. Natl Acad. Sci. USA **106**, 22287–22292 (2009).
10. C. J. R. Sheppard, S. B. Mehta, and R. Heintzmann, “Superresolution by image scanning microscopy using pixel reassignment,” Opt. Lett. **38**, 2889–2892 (2013).
11. J. Huff, “The Airyscan detector from ZEISS: confocal imaging with improved signal-to-noise ratio and super-resolution,” Nat. Methods **12**, i–ii (2015).
12. I. Gregor and J. Enderlein, “Image scanning microscopy,” Curr. Opin. Chem. Biol. **51**, 74–83 (2019).
13. G. M. R. De Luca, R. M. P. Breedijk, R. A. J. Brandt, C. H. C. Zeelenberg, B. E. de Jong, W. Timmermans, L. Nahidi Azar, R. A. Hoebe, S. Stallinga, and E. M. M. Manders, “Re-scan confocal microscopy: scanning twice for better resolution,” Biomed. Opt. Express **4**, 2644–2656 (2013).
14. S. Roth, C. J. R. Sheppard, K. Wicker, and R. Heintzmann, “Optical photon reassignment microscopy (OPRA),” Opt. Nanosc. **2**, 5 (2013).

15. C. Roider, R. Piestun, and A. Jesacher, “3D image scanning microscopy with engineered excitation and detection,” Optica **4**, 1373–1381 (2017).
16. F. Strasser, M. Offterdinger, R. Piestun, and A. Jesacher, “Spectral image scanning microscopy,” Biomed. Opt. Express **10**, 2513–2527 (2019).
17. I. Gregor, M. Spiecker, R. Petrovsky, J. Großhans, R. Ros, and J. Enderlein, “Rapid nonlinear image scanning microscopy,” Nat. Methods **14**, 1087–1089 (2017).
18. O. Tzang, D. Feldkhun, A. Agrawal, A. Jesacher, and R. Piestun, “Two-photon PSF-engineered image scanning microscopy,” Opt. Lett. **44**, 895–898 (2019).
19. M. Ingaramo, A. G. York, P. Wawrzusin, O. Milberg, A. Hong, R. Weigert, H. Shroff, and G. H. Patterson, “Two-photon excitation improves multifocal structured illumination microscopy in thick scattering tissue,” Proc. Natl Acad. Sci. USA **111**, 5254–5259 (2014).
20. S. V. Koho, E. Slenders, G. Tortarolo, M. Castello, M. Buttafava, F. Villa, E. Tcarenkova, M. Ameloot, P. Bianchini, C. J. R. Sheppard, A. Diaspro, A. Tosi, and G. Vicidomini, “Two-photon image-scanning microscopy with SPAD array and blind image reconstruction,” Biomed. Opt. Express **11**, 2905–2924 (2020).
21. C. Roider, M. Ritsch-Marte, and A. Jesacher, “High-resolution confocal Raman microscopy using pixel reassignment,” Opt. Lett. **41**, 3825–3828 (2016).
22. M. Castello, G. Tortarolo, M. Buttafava, T. Deguchi, F. Villa, S. Koho, L. Pesce, M. Oneto, S. Pelicci, L. Lanzanó, P. Bianchini, C. J. R. Sheppard, A. Diaspro, A. Tosi, and G. Vicidomini, “A robust and versatile platform for image scanning microscopy enabling super-resolution FLIM,” Nat. Methods **16**, 175–178 (2019).
23. T. B. DuBose, F. LaRocca, S. Farsiu, and J. A. Izatt, “Super-resolution retinal imaging using optically reassigned scanning laser ophthalmoscopy,” Nat. Photonics **13**, 257–262 (2019).
24. G. P. J. Laporte, N. Stasio, C. J. R. Sheppard, and D. Psaltis, “Resolution enhancement in nonlinear scanning microscopy through post-detection digital computation,” Optica **1**, 455–460 (2014).
25. R. Tenne, U. Rossman, B. Rephael, Y. Israel, A. Krupinski-Ptaszek, R. Lapkiewicz, Y. Silberberg, and D. Oron, “Super-resolution enhancement by quantum image scanning microscopy,” Nat. Photonics **13**, 116–122 (2019).
26. G. Lubin, R. Tenne, I. M. Antolovic, E. Charbon, C. Bruschini, and D. Oron, “Quantum correlation measurement with single photon avalanche diode arrays,” Opt. Express **27**, 32863–32882 (2019).
27. U. Rossman, R. Tenne, O. Solomon, I. Kaplan-Ashiri, T. Dadosh, Y. C. Eldar, and D. Oron, “Rapid quantum image scanning microscopy by joint sparse reconstruction,” Optica **6**, 1290–1296 (2019).
28. P. Dedecker, G. C. H. Mo, T. Dertinger, and J. Zhang, “Widely accessible method for superresolution fluorescence imaging of living systems,” Proc. Natl Acad. Sci. USA **109**, 10909–10914 (2012).
29. T. Dertinger, M. Heilemann, R. Vogel, M. Sauer, and S. Weiss, “Superresolution optical fluctuation imaging with organic dyes,” Angew. Chem. (Int. Ed.) **49**, 9441–9443 (2010).
30. S. Duwé, E. De Zitter, V. Gielen, B. Moeyaert, W. Vandenberg, T. Grotjohann, K. Clays, S. Jakobs, L. Van Meervelt, and P. Dedecker, “Expression-enhanced fluorescent proteins based on enhanced green fluorescent protein for super-resolution microscopy,” ACS Nano **9**, 9528–9541 (2015).
31. X. Zhang, X. Chen, Z. Zeng, M. Zhang, Y. Sun, P. Xi, J. Peng, and P. Xu, “Development of a reversibly switchable fluorescent protein for super-resolution optical fluctuation imaging (SOFI),” ACS Nano **9**, 2659–2667 (2015).
32. G. Zhao, C. Zheng, C. Kuang, and X. Liu, “Resolution-enhanced SOFI via structured illumination,” Opt. Lett. **42**, 3956–3959 (2017).
33. A. Classen, J. von Zanthier, M. O. Scully, and G. S. Agarwal, “Superresolution via structured illumination quantum correlation microscopy,” Optica **4**, 580–587 (2017).
34. G. M. R. De Luca, “Re-scan confocal microscopy,” Ph.D. thesis (University of Amsterdam, 2016).
35. O. Schwartz, J. M. Levitt, R. Tenne, S. Itzhakov, Z. Deutsch, and D. Oron, “Superresolution microscopy with quantum emitters,” Nano Lett. **13**, 5832–5836 (2013).
36. P. Spinicelli, S. Buil, X. Quélin, B. Mahler, B. Dubertret, and J.-P. Hermier, “Bright and grey states in CdSe-CdS nanocrystals exhibiting strongly reduced blinking,” Phys. Rev. Lett. **102**, 136801 (2009).
37. W. Qin, R. A. Shah, and P. Guyot-Sionnest, “CdSeS/ZnS alloyed nanocrystal lifetime and blinking studies under electrochemical control,” ACS Nano **6**, 912–918 (2012).
38. R. Tenne, A. Teitelboim, P. Rukenstein, M. Dyshel, T. Mokari, and D. Oron, “Studying quantum dot blinking through the addition of an engineered inorganic hole trap,” ACS Nano **7**, 5084–5090 (2013).
39. S. C. Stein, “Advanced data processing in super-resolution microscopy,” Ph.D. thesis (Georg-August-Universität Göttingen, 2017).
40. W. Vandenberg, M. Leutenegger, S. Duwé, and P. Dedecker, “An extended quantitative model for super-resolution optical fluctuation imaging (SOFI),” Opt. Express **27**, 25749–25766 (2016).
41. S. Geissbuehler, N. L. Bocchio, C. Dellagiacoma, C. Berclaz, M. Leutenegger, and T. Lasser, “Mapping molecular statistics with balanced super-resolution optical fluctuation imaging (bSOFI),” Opt. Nanosc. **1**, 4–7 (2012).
42. S. Jiang, Y. Zhang, H. Yang, Y. Xiao, X. Miao, R. Li, Y. Xu, and X. Zhang, “Enhanced SOFI algorithm achieved with modified optical fluctuating signal extraction,” Opt. Express **24**, 3037–3045 (2016).
43. O. Solomon, M. Mutzafi, M. Segev, and Y. C. Eldar, “Sparsity-based super-resolution microscopy from correlation information,” Opt. Express **26**, 18238–18269 (2018).
44. X. Yi, S. Son, R. Ando, A. Miyawaki, and S. Weiss, “Moments reconstruction and local dynamic range compression of high order superresolution optical fluctuation imaging,” Biomed. Opt. Express **10**, 2430–2445 (2019).
45. N. Gustafsson, S. Culley, G. Ashdown, D. M. Owen, P. M. Pereira, and R. Henriques, “Fast live-cell conventional fluorophore nanoscopy with ImageJ through super-resolution radial fluctuations,” Nat. Commun. **7**, 12471 (2016).
46. K. Agarwal and R. Macháň, “Multiple signal classification algorithm for super-resolution fluorescence microscopy,” Nat. Commun. **7**, 13752 (2016).
47. B. Wang, L. Yao, Y. Jing, Y. Fei, Q. Bai, L. Mi, and J. Ma, “Multicomposite super-resolution microscopy: enhanced Airyscan resolution with radial fluctuation and sample expansions,” J. Biophoton. **13**, e2419 (2020).
48. B. Moeyaert, N. Nguyen Bich, E. De Zitter, S. Rocha, K. Clays, H. Mizuno, L. van Meervelt, J. Hofkens, and P. Dedecker, “Green-to-red photoconvertible dronpa mutant for multimodal super-resolution fluorescence microscopy,” ACS Nano **8**, 1664–1673 (2014).
49. T. Ha and P. Tinnefeld, “Photophysics of fluorescent probes for single-molecule biophysics and super-resolution imaging,” Annu. Rev. Phys. Chem. **63**, 595–617 (2012).
50. A. G. York, S. H. Parekh, D. Dalle Nogare, R. S. Fischer, K. Temprine, M. Mione, A. B. Chitnis, C. A. Combs, and H. Shroff, “Resolution doubling in live, multicellular organisms via multifocal structured illumination microscopy,” Nat. Methods **9**, 749–754 (2012).
51. C. Bruschini, H. Homulle, I. M. Antolovic, S. Burri, and E. Charbon, “Single-photon avalanche diode imagers in biophotonics: review and outlook,” Light Sci. Appl. **8**, 87 (2019).
52. A. Classen, J. von Zanthier, and G. S. Agarwal, “Analysis of super-resolution via 3D structured illumination intensity correlation microscopy,” Opt. Express **26**, 27492–27503 (2018).
53. E. Mudry, K. Belkebir, J. Girard, J. Savatier, E. Le Moal, C. Nicoletti, M. Allain, and A. Sentenac, “Structured illumination microscopy using unknown speckle patterns,” Nat. Photonics **6**, 312–315 (2012).
54. R. Ayuk, H. Giovannini, A. Jost, E. Mudry, J. Girard, T. Mangeat, N. Sandeau, R. Heintzmann, K. Wicker, K. Belkebir, and A. Sentenac, “Structured illumination fluorescence microscopy with distorted excitations using a filtered blind-SIM algorithm,” Opt. Lett. **38**, 4723–4726 (2013).
55. S. Labouesse, A. Negash, J. Idier, S. Bourguignon, T. Mangeat, P. Liu, A. Sentenac, and M. Allain, “Joint reconstruction strategy for structured illumination microscopy with unknown illuminations,” IEEE Trans. Image Process. **26**, 2480–2493 (2017).
56. A. Negash, S. Labouesse, N. Sandeau, M. Allain, H. Giovannini, J. Idier, R. Heintzmann, P. C. Chaumet, K. Belkebir, and A. Sentenac, “Improving the axial and lateral resolution of three-dimensional fluorescence microscopy using random speckle illuminations,” J. Opt. Soc. Am. A **33**, 1089–1094 (2016).
57. L. H. Yeh, L. Tian, and L. Waller, “Structured illumination microscopy with unknown patterns and a statistical prior,” Biomed. Opt. Express **8**, 695–711 (2017).
58. M. Kim, C. Park, C. Rodriguez, Y. Park, and Y. Cho, “Superresolution imaging with optical fluctuation using speckle patterns illumination,” Sci. Rep. **5**, 16525 (2015).